analytical chemistry

pubs.acs.org/ac Article

Copper-Doped Terbium Luminescent Metal Organic Framework as an Emitter and a Co-reaction Promoter for Amplified Electrochemiluminescence Immunoassay

Chao Wang, Zhaohui Li, and Huangxian Ju*

Cite This: *Anal. Chem.* 2021, 93, 14878−14884 Read Online

ACCESS | Metrics & More | Article Recommendations | Supporting Information

ABSTRACT: This work designed a signal amplification strategy for construction of a highly sensitive electrochemiluminescence (ECL) biosensor by doping Cu^{2+} in a terbium luminescent metal organic framework (Cu:Tb-MOF) to act as a co-reaction promoter, which enhanced the generation of $SO_4^{\bullet-}$ radical during the cathodic process in the presence of $K_2S_2O_8$ as a co-reactant. The porous and hollow morphology and the size of Cu:Tb-MOF could be efficiently tuned via changing the molar ratio of Cu^{2+} and Tb^{3+} and the reaction time, which were related to the specific surface area, pore diameter, and the ECL intensity of the MOF structure. To further improve the sensitivity of the ECL biosensor, H_2O_2 was introduced into the ECL system to act as another co-reaction promoter, leading to a new ECL mechanism involving dual co-reaction promoters. In view of the low electron transfer resistance of Cu:Tb-MOF, a label-free ECL immunosensor was conveniently constructed by co-immobilizing Cu:Tb-MOF and the capture antibody on the electrode surface. Using pro-gastrin-releasing peptide (ProGRP, a biomarker of small-cell lung cancer) as the model target, the proposed immunosensor exhibited excellent performance with a detection range of 1.0 pg·mL^{-1} to 50 ng·mL^{-1} and a limit of detection down to 0.68 pg·mL^{-1} (3σ). This work demonstrated a strategy to use the MOF structures as both an emitter and a co-reaction promoter for amplified ECL emission and proposed an innovative route to extend the application of lanthanide MOFs.

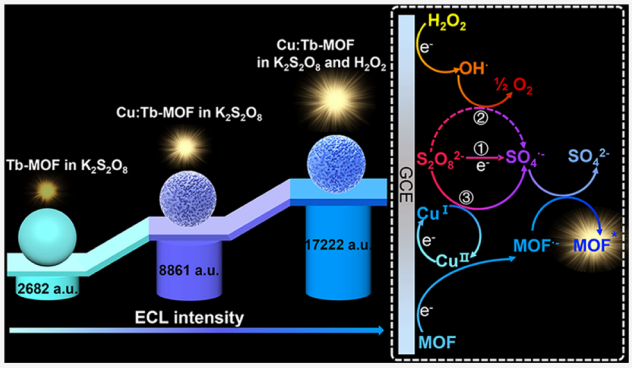

INTRODUCTION

With the merits of negligible background and electrochemical controllability, electrochemiluminescence (ECL) detection has become an exuberant analytical technology in different fields including clinical diagnostics and disease prognosis.[1] Over the past few decades, the list of ECL emitters has been extended from typical reagents such as luminol and $Ru(bpy)_3^{2+}$ to quantum dots;[2] polymer dots;[3] metal nanoclusters;[4] and a large number of nanocomposites of nanomaterials, such as carbon nanotubes,[5] ordered mesoporous carbon,[6] Au nanoparticles,[7] silica nanoparticles,[8] polymer dots,[9] and metal organic frameworks (MOFs),[10−12] loaded with luminol or $Ru(bpy)_3^{2+}$. However, the application of these ECL nanocomposites, particularly $Ru(bpy)_3^{2+}$- or luminol-loaded MOFs, is greatly limited due to the leakage of small luminescence components, which influences seriously the stability of ECL emission and the accuracy of analysis. Therefore, the self-ECL properties of nanomaterials have attracted considerable attention.[13−15] Among these self-ECL nanomaterials, lanthanide MOFs hold great application prospects due to their long decay lifetime (~ms) and high luminescence efficiency.[16−18] By introducing appropriate organic ligands, these ECL behaviors can be conveniently tuned by the antenna effect or the intramolecular energy transfer, while the low quantum yield of lanthanide elements due to the parity-forbidden f−f transitions can also be circumvented.[19] However, most ECL studies on lanthanide MOFs mainly focus on europium-based MOFs (Eu-MOFs),[16−18] and the investigation of terbium-based MOFs (Tb-MOFs) is still in its infancy as the luminescence performance of Tb^{3+} is inferior to that of Eu^{3+}. Hence, exploration of effective and convenient ECL signal amplification strategies is highly desired for the application of Tb-MOFs in ECL bioassay.

Currently, co-reaction promoter has been developed as an effective strategy to promote the decomposition of co-reactant and thus amplify the ECL signal.[20] Various nanomaterials, such as Ti_3C_3 nanosheets,[21] $CoFe_2O_4$ nanoparticles,[22] Fe_3O_4-CeO_2 nanocomposites,[23] and silver nanoflowers,[24] have been employed as the co-reaction promoters of $K_2S_2O_8$ to enhance

Received: September 13, 2021
Accepted: October 19, 2021
Published: October 27, 2021

https://doi.org/10.1021/acs.analchem.1c03988
Anal. Chem. 2021, 93, 14878−14884

the generation of $SO_4^{\bullet-}$ radical during the cathodic process. In addition, some electroactive reagents, such as hemin[25] and Bu_4NPF_6,[26] have been added in $K_2S_2O_8$ solution to act as co-reaction promoters. In these ECL systems, the emitter and the co-reaction promoter are usually not in the single nanostructure, which increases the distance between the emitter and the strong oxidizing intermediate ($SO_4^{\bullet-}$) and thus causes energy loss.[27] To shorten the distance between emitters and $SO_4^{\bullet-}$, the doping of metal ions during the preparation of ECL emitters to act as the co-reaction promoters has been proposed. For example, a Eu-doped phosphoric acid gadolinium nanorod has been reported as a low-potential ECL emitter to construct an ultrasensitive ECL immunosensor.[28] In this work, a dual co-reaction promoting strategy was designed using Cu^{2+} doping and H_2O_2 to increase the amount of electrochemically generated $SO_4^{\bullet-}$ radical[29] for amplifying the ECL emission of Tb-MOF.

The Cu^{2+}-doped Tb-MOF (Cu:Tb-MOF) prepared with isophthalic acid (IPA) as the ligand of metal ions could act as both the ECL emitter and the co-reaction promoter. Its morphology and size could be efficiently tuned via changing the molar ratio of Cu^{2+} and Tb^{3+} and the reaction time for its preparation. The porous and hollow structure and high Brunauer−Emmett−Teller (BET) surface area endowed Cu:Tb-MOF with low electron transfer resistance and the access of active intermediates to react with more emitters for ECL signal amplification. As a proof of concept of the analytical application, a label-free ECL immunosensor was constructed for detection of pro-gastrin-releasing peptide (ProGRP),[30] a promising biomarker of small-cell lung cancer with a threshold value of 50 pg·mL^{-1},[31] by co-immobilizing Cu:Tb-MOF and the capture antibody on the electrode surface. The excellent performance of the proposed immunosensor demonstrated the application potential of lanthanide MOFs and dual co-reaction promoters in ECL bioassay.

EXPERIMENTAL SECTION

Materials, Reagents, and Apparatus. Detailed information is described in the Supporting Information (SI).

Preparation of Tb-MOF and Cu:Tb-MOF. Tb-MOF and Cu:Tb-MOF were synthesized via the method described previously[32] with some modification. For the preparation of Tb-MOF, 24 mL of $Tb(NO_3)_3$ solution (20 mM) was added to 30 mL of *N*,*N*-dimethylformamide (DMF) and mixed with 12 mL of DMF solution of IPA (0.0797 g) and stirred for 20 min. After the mixture was transferred into a 100 mL Teflon-lined stainless steel autoclave to react at 160 °C for 3 h, the autoclave was cooled to room temperature, and the white sediment was isolated by centrifugation at 8000 rpm for 5 min and washed with ethanol six times. The product was dried in a 60 °C vacuum oven overnight. Different Cu:Tb-MOFs were prepared via changing the dosage of $Cu(NO_3)_2$ and solvothermal reaction time.

Fabrication of the ECL Immunosensor. After the glassy carbon electrode (GCE) was polished with alumina slurry (0.05 μm) and washed ultrasonically with water, ethanol, and water for 5 min, respectively, 20 μL of 2 mg·mL^{-1} Cu:Tb-MOF obtained at the Cu/Tb ratio of 1.5:1 with a reaction time of 9 h was coated on its surface and dried at 37 °C to obtain a MOF-modified electrode. The electrode was then coated with 10 μL of chitosan (CS, 0.25 mg·mL^{-1}) and 10 μL of glutaraldehyde (GA, 2.5 v/v %) successively to react for 30 min at 37 °C. Afterward, 20 μL of anti-ProGRP antibody (Ab, 10 μg·mL^{-1}) was dropped on the surface to incubate at 4 °C for 12 h, followed by washing with phosphate buffer saline (PBS, pH 7.4) and then treating with 10 μL of bovine serum albumin (BSA, 0.1 wt %) for 40 min to prevent nonspecific adsorption. After washing the surface with PBS, the immunosensor for ProGRP was obtained. The fabrication and detection processes of the immunosensor for ProGRP are depicted in Scheme 1A.

Scheme 1. Schematic Diagram of (A) Immunosensor Fabrication and (B) the ECL Mechanism

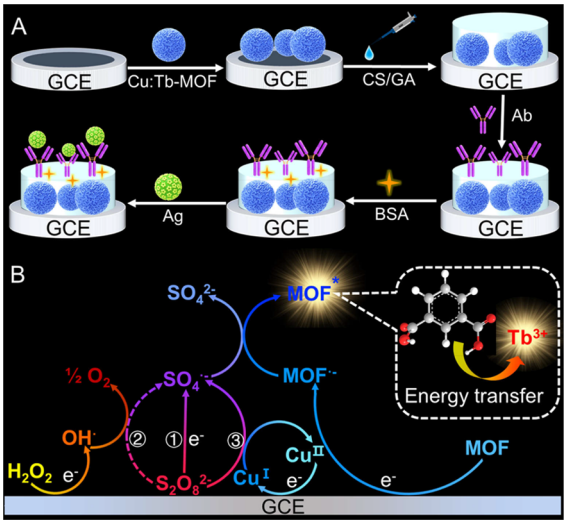

ECL Detection of ProGRP. After 20 μL of ProGRP with different concentrations or the samples was incubated on the immunosensor at 37 °C for 1 h, the GCE was rinsed with PBS and applied for ECL measurement in 0.1 M pH 7.4 PBS containing 0.1 M $K_2S_2O_8$, 0.1 M KCl, and 20 mM H_2O_2 by scanning the potential from 0 to −1.8 V at 100 mV·s^{-1}.

RESULTS AND DISCUSSION

Characterizations of Tb-MOF and Cu:Tb-MOF. The scanning electron microscopy (SEM) and transmission electron microscopy (TEM) images of Tb-MOF showed a smooth and solid spherical structure with a diameter of around 1200 nm (Figure 1B). In comparison with Tb-MOF, Cu:Tb-MOF became smaller and its surface was also rougher (Figure 1C,D). Moreover, the structure of MOF changed from solid to hollow with abundant micropores after Cu^{2+} doping (Figure 1E). The thickness of the MOF shell was about 150 nm. The TEM mappings (Figure 1F) and energy-dispersive spectrum (Figure S1) revealed that Cu:Tb-MOF was composed of Cu, Tb, C, and O (not shown in the mapping) elements. The perfect overlap of Cu^{2+} and Tb^{3+} mappings showed the uniform distribution of Cu^{2+} and Tb^{3+} in Cu:Tb-MOF via coordination with the carboxyl group of IPA.

The X-ray photoelectron spectrum (XPS) of Cu:Tb-MOF indicated the presence of Cu 2p, Tb 4d, C 1s, and O 1s (Figure S2A). The Cu 2p pattern exhibited two intense peaks at 951.9 and 932.1 eV for Cu $2p_{1/2}$ and Cu $2p_{3/2}$, respectively, a satellite peak at 943.1 eV (Figure S2B), and an Auger peak at 569.8 eV in the Cu LMM region (Figure S2C), confirming the presence of Cu^{2+}.[33] The Fourier transform infrared (FT-IR) spectra demonstrated the coordination between IPA and Cu^{2+} or Tb^{3+}, which led to the shift of the symmetric stretching vibration

https://doi.org/10.1021/acs.analchem.1c03988
Anal. Chem. 2021, 93, 14878−14884

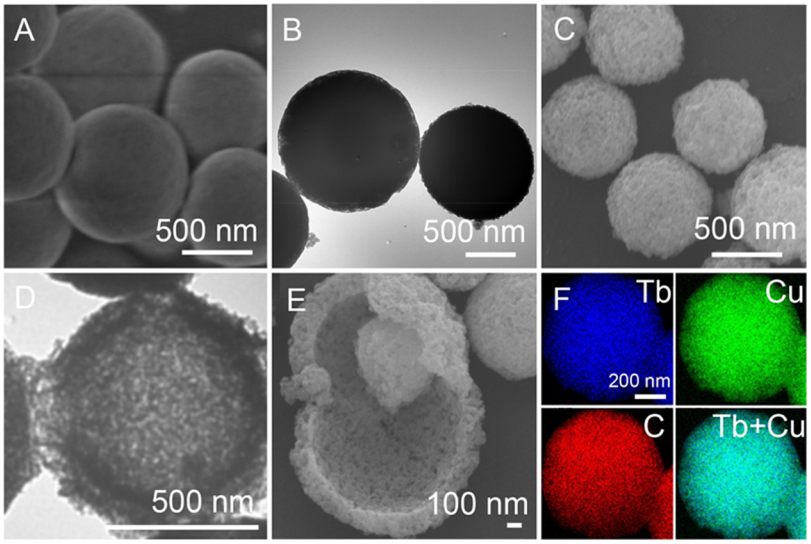

Figure 1. (A) SEM and (B) TEM images of Tb-MOF. (C) SEM and (D) TEM images of Cu:Tb-MOF. (E) SEM image of broken Cu:Tb-MOF. (F) TEM mapping of Cu:Tb-MOF. Cu:Tb-MOF was prepared with the Cu/Tb molar ratio of 1.5:1 and reaction time of 9 h.

band of COO^- from 1418 cm^{-1} of IPA[17] to 1398 cm^{-1} of Tb-MOF and 1391 cm^{-1} of Cu:Tb-MOF due to the decreased force constants of COO^- in the presence of Cu^{2+} or Tb^{3+}, and enhanced the asymmetric stretching vibration band of COO^- at 1580 cm^{-1} (Figure S2D). The strong band assigned to the stretching vibration of C═O shifted from 1690 cm^{-1} of IPA to 1655 cm^{-1} of the MOFs due to the coordination of the carboxyl group with Cu^{2+} and Tb^{3+}.[32] Thermogravimetric analysis of Cu:Tb-MOF (Figure S2E) suggested that the sample remained thermally stable up to 500 °C. The amorphous structure of Cu:Tb-MOF was also verified from the powder X-ray diffraction (PXRD) pattern of Cu:Tb-MOF, which did not show a well-defined diffraction peak, except for the two weak peaks at around 35−45° (Figure S2F).

A strong absorption band centered at 293 nm was observed in the ultraviolet and visible (UV−vis) absorption spectrum of IPA owing to the ligand-centered $\pi-\pi^*$ transition (Figure 2A).

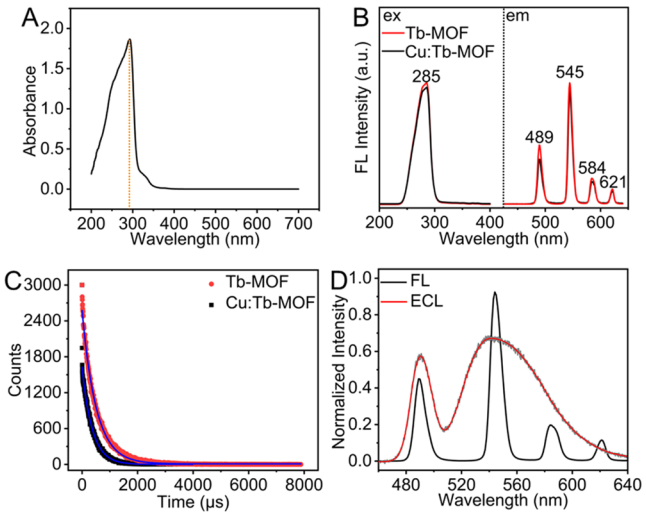

Figure 2. (A) UV−vis absorption spectrum of IPA. (B, C) FL excitation and emission spectra (B) and time-resolved decay curves (C) of Tb-MOF and Cu:Tb-MOF. (D) ECL spectrum of Cu:Tb-MOF compared with its FL emission spectrum.

The fluorescence (FL) excitation peaks of Tb-MOF and Cu:Tb-MOF were positioned at 285 nm, which were close to the absorption peak of IPA, suggesting that the Tb^{3+} emission could be achieved via the energy transfer from IPA to Tb^{3+}.[34] Their FL emission spectra displayed four characteristic emission peaks of Tb^{3+} at 489, 545, 584, and 621 nm, corresponding to the $^5D_4$ to $^7F^6$, $^7F_5$, $^7F_4$, and $^7F_3$ transitions, respectively (Figure 2B).[35] The time-resolved decay curves of Tb-MOF and Cu:Tb-MOF at the excitation wavelength of 285 nm (Figure 2C) showed the relatively long luminescence lifetimes of 0.51 and 0.37 ms for Tb-MOF and Cu:Tb-MOF, respectively. The ECL spectrum of Cu:Tb-MOF (Figure 2D) showed two strong emission peaks at around 490 and 545 nm, which were similar to the two intense FL peaks, indicating that the ECL behavior of Cu:Tb-MOF originated from the intramolecular energy transfer from IPA to Tb^{3+}.[36] Moreover, both ECL peaks of Cu:Tb-MOF were different from that of the $O_2/K_2S_2O_8$ system at 575 nm,[25,37] implying that Cu:Tb-MOF was the ECL emitter.

Electrochemical and ECL Behaviors of Cu:Tb-MOF. The cyclic voltammograms (CVs) of IPA/GCE, Tb-MOF/GCE, and Cu:Tb-MOF/GCE in 0.1 M pH 7.4 PBS exhibited an irreversible reduction peak at about −1.4 V (Figure 3A, curves b−d), indicating the same reduction process of the MOFs as the IPA ligand. The bare GCE showed the reduction peak of $K_2S_2O_8$ at −1.20 V, which shifted to −1.40 V and overlapped with the IPA reduction at IPA/GCE (Figure 3B, curves a,b), indicating the inhibition of IPA to $S_2O_8^{2-}$ reduction due to the negatively charged surface. At Tb-MOF/GCE, the reduction peak of $S_2O_8^{2-}$ positively shifted to −1.12 V (Figure 3B, curve c), indicating that the porous MOF structure was conducive to the reduction of $S_2O_8^{2-}$. The reduction peak further shifted to −1.06 V at Cu:Tb-MOF/GCE (Figure 3B, curve d), indicating that the doping of Cu^{2+} could promote the reduction of $K_2S_2O_8$. Moreover, the presence of $S_2O_8^{2-}$ did not affect the electrochemical reduction of IPA in both Tb-MOF/GCE and Cu:Tb-MOF/GCE at about −1.4 V(Figure 3B, curves c,d).

The $S_2O_8^{2-}$ solution showed weak ECL emission at bare GCE, as reported previously,[15] which increased at IPA/GCE (Figure 3C, curves a,b), indicating that IPA participated in the

https://doi.org/10.1021/acs.analchem.1c03988
Anal. Chem. 2021, 93, 14878−14884

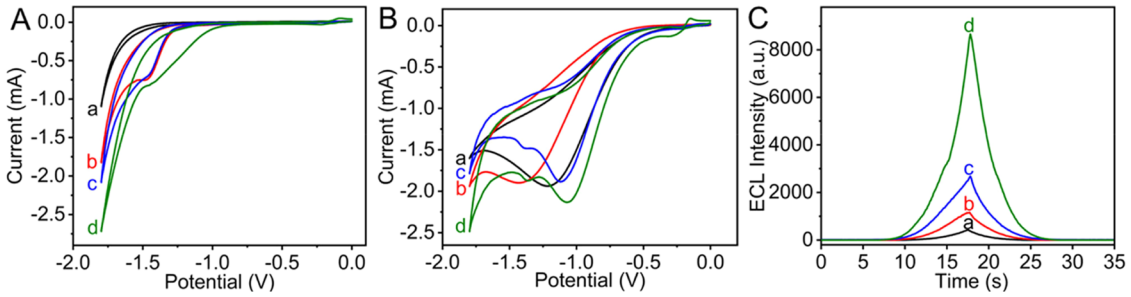

Figure 3. (A, B) CV curves of (a) GCE, (b) IPA/GCE, (c) Tb-MOF/GCE, and (d) Cu:Tb-MOF/GCE in 0.1 M pH 7.4 PBS in the absence (A) and presence (B) of 0.1 M $K_2S_2O_8$. (C) ECL−time curves of (a) GCE, (b) IPA/GCE, (c) Tb-MOF/GCE, and (d) Cu:Tb-MOF/GCE in 0.1 M pH 7.4 PBS containing 0.1 M $K_2S_2O_8$.

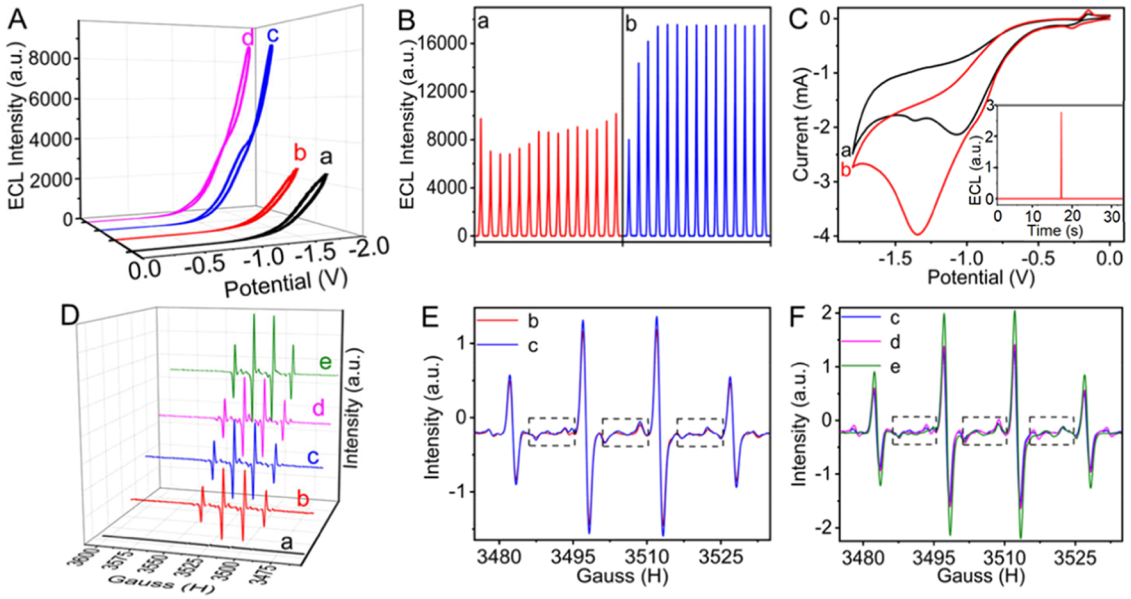

Figure 4. (A) ECL−potential curves of (a, b) Tb-MOF/GCE and (c, d) Cu:Tb-MOF/GCE in (a, c) air-saturated and (b, d) N_2-saturated 0.1 M pH 7.4 PBS containing 0.1 M $K_2S_2O_8$. (B) ECL−time curves and (C) CV curves of Cu:Tb-MOF/GCE in 0.1 M pH 7.4 PBS containing 0.1 M $K_2S_2O_8$ in the absence (a) and presence (b) of 20 mM H_2O_2. (D−F) EPR spectra of (a) Cu:Tb-MOF/GCE in 0.1 M pH 7.4 PBS containing 100 mM DMPO, (b) Tb-MOF/GCE, and (c−e) Cu:Tb-MOF/GCE in 0.1 M pH 7.4 PBS containing 0.1 M $K_2S_2O_8$ and 100 mM DMPO in the absence (b, c) and presence of 20 (d) or 40 (e) mM H_2O_2 at −1.8 V for 150 s. The inset in (C) shows the ECL−time curve of Cu:Tb-MOF/GCE in 0.1 M pH 7.4 PBS containing 20 mM H_2O_2.

ECL process. This ECL emission further increased at Tb-MOF/GCE (Figure 3C, curve c), which was attributed to the effective energy transfer from the excited IPA to Tb^{3+}, as demonstrated in Figure 2D.[36] After Cu^{2+} doping, Cu:Tb-MOF/GCE exhibited a significant ECL enhancement (Figure 3C, curve d).

ECL Mechanism of Cu:Tb-MOF. In the cathodic process, $S_2O_8^{2-}$ and Cu:Tb-MOF (denoted as Cu:Tb-IPA for clear description here) were reduced to form $SO_4^{\bullet-}$ and Cu:Tb-IPA$^{\bullet-}$, respectively (Figure 3B, curve d) (eqs 1 and 2). The formed Cu:Tb-IPA$^{\bullet-}$ was then oxidized by the intermediate $SO_4^{\bullet-}$ to produce Cu:Tb-IPA* (eq 3), corresponding to the singlet state (S_1) of IPA (Scheme S1). According to Reinhold's empirical rule,[38] the excitation energy of Cu:Tb-IPA* could be transferred from S_1 (32790 cm^{-1}) to T_1 (25060 cm^{-1}) of IPA via intersystem crossing (ISC) due to the energy difference (ΔE_1) being larger than 5000 cm^{-1},[39] and then the excitation energy of Cu:Tb-IPA* could be intramolecularly transferred from T_1 of IPA to $^5D_4$ of Tb^{3+} (20 500 cm^{-1}) due to their energy difference (ΔE_2) being larger than 4000 cm^{-1},[39] leading to the generation of Cu:Tb*-IPA (eq 4) and the ECL emission from $^5D_4$ to ^7F_J (J = 6, 5, 4, 3) of Tb^{3+} (eq 5).[36] Thus, the ECL mechanism of Cu:Tb-MOF in the presence of $S_2O_8^{2-}$ could be described as follows

$$S_2O_8^{2-} + e^- \rightarrow SO_4^{\bullet-} + SO_4^{2-} \quad (1)$$

$$\text{Cu: Tb} - \text{IPA} + e^- \rightarrow \text{Cu: Tb} - \text{IPA}^{\bullet-} \quad (2)$$

$$\text{Cu: Tb} - \text{IPA}^{\bullet-} + SO_4^{\bullet-} \rightarrow \text{Cu: Tb} - \text{IPA}^* + SO_4^{2-} \quad (3)$$

$$\text{Cu: Tb} - \text{IPA}^* \rightarrow \text{Cu: Tb}^* - \text{IPA} \quad (4)$$

$$\text{Cu: Tb}^* - \text{IPA} \rightarrow \text{Cu: Tb} - \text{IPA} + h\nu \quad (5)$$

Signal Amplification Mechanism. Besides the irreversible reduction peak of the IPA ligand at about −1.4 V, the CV of Cu:Tb-MOF/GCE showed a couple of redox peaks at around −0.10 and −0.22 V (Figure 3A, curve d), which could be attributed to the reduction and oxidation of the Cu^{2+}/Cu^+ couple. In the presence of $S_2O_8^{2-}$, the redox peak potentials of the Cu^{2+}/Cu^+ couple became about −0.16 and −0.28 V, and the reduction peak current greatly increased (Figure 3B, curve

https://doi.org/10.1021/acs.analchem.1c03988
Anal. Chem. 2021, 93, 14878−14884

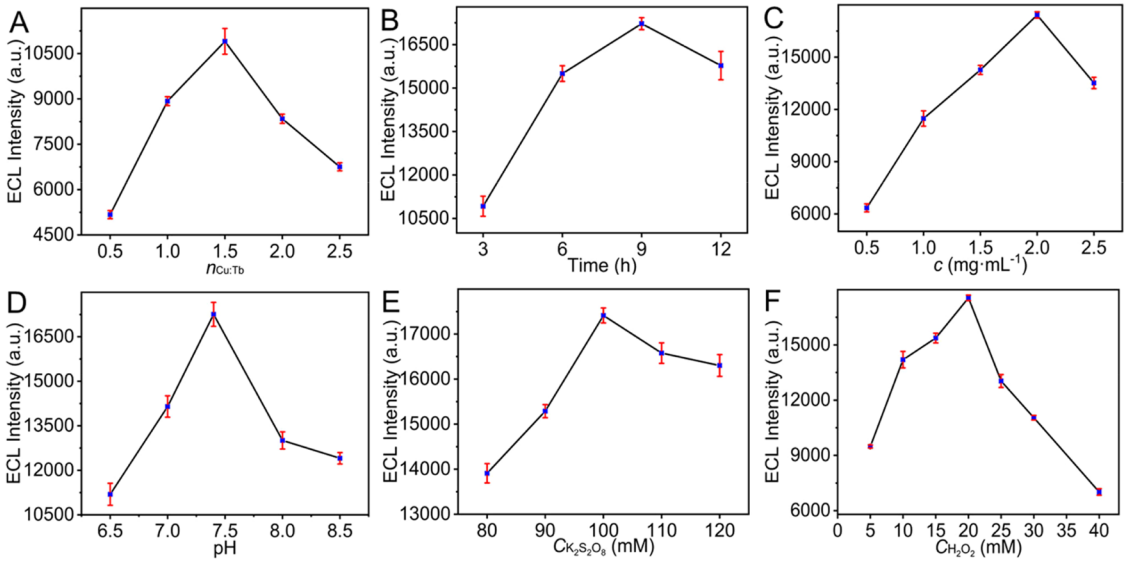

Figure 5. Effects of the (A) molar ratio of Cu^{2+} and Tb^{3+} and (B) reaction time for preparation of Cu:Tb-MOF, (C) amount of Cu:Tb-MOF for preparation of the modified electrode, (D) pH of PBS, (E) $K_2S_2O_8$, and (F) H_2O_2 concentration on the ECL intensity of Cu:Tb-MOF/GCE (n = 3). (B)−(F): when one parameter changed, the others were at their optimal conditions.

d), indicating that $S_2O_8^{2-}$ catalyzed the electrochemical reduction of the Cu^{2+}/Cu^{+} couple. The formation of the electrocatalytic product $SO_4^{\bullet-}$[40] resulted in the enhancement of the ECL emission by three times (Figures 3C and 4A), which was unaffected by the presence of dissolved oxygen (Figure 4A), indicating a negligible effect of dissolved oxygen on the cathodic ECL process due to the presence of $S_2O_8^{2-}$ with relatively high concentration. Thus, Cu^{2+} in Cu:Tb-MOF could be considered as a co-reaction promoter in the ECL system,[40,41] and the electrocatalytic process could be described with eqs 6 and 7, in which the produced $SO_4^{\bullet-}$ enhanced the ECL emission through reactions 3−5.

$$Cu^{II} + e^{-} \rightarrow Cu^{I} \quad (6)$$

$$Cu^{I} + S_2O_8^{2-} \rightarrow Cu^{II} + SO_4^{2-} + SO_4^{\bullet-} \quad (7)$$

After introducing 20 mM H_2O_2 into 0.1 M $K_2S_2O_8$, the ECL intensity of Cu:Tb-MOF/GCE further increased, and the ECL signal turned out to be highly stable after cyclic scanning for four cycles (Figure 4B, curve b). Meanwhile, the CV curve of Cu:Tb-MOF/GCE retained the redox peaks of the Cu^{2+}/Cu^{+} couple with slightly increased peak currents, and the cathodic curve showed a great reduction peak at −1.35 V with a shoulder at around −0.9 V (Figure 4C, curve b), which could be attributed to the overlap of the reduction peaks of H_2O_2, Cu:Tb-IPA, and $S_2O_8^{2-}$. In the absence of $S_2O_8^{2-}$, Cu:Tb-MOF/GCE showed negligible ECL emission in 0.1 M pH 7.4 PBS containing 20 mM H_2O_2 (inset in Figure 4C), indicating that H_2O_2 could not act as the co-reactant, which was different from the dual co-reactants.[42] Therefore, the gradually increased ECL signal in the first four cycles (Figure 4B, curve b) implied that the electroreduction product of H_2O_2 (eq 8) catalyzed the reduction of $S_2O_8^{2-}$ to produce more $SO_4^{\bullet-}$ (eq 9).[31] It is worth noting that excess H_2O_2 could lead to the decrease of the ECL intensity due to the scavenging of $SO_4^{\bullet-}$ by $OH^{\bullet}$ (eq 10).[43] As a result, appropriate H_2O_2 acted as another co-reaction promoter of $S_2O_8^{2-}$ to amplify the ECL signal of Tb-MOF. The ECL signal amplification mechanism involving dual co-reaction promoters is depicted in Scheme 1B.

$$H_2O_2 + e^{-} \rightarrow OH^{\bullet} + OH^{-\bullet} \quad (8)$$

$$S_2O_8^{2-} + OH^{\bullet} \rightarrow SO_4^{\bullet-} + HSO_4^{-} + 1/2O_2 \quad (9)$$

$$OH^{\bullet} + SO_4^{\bullet-} \rightarrow HSO_4^{\bullet-} + 1/2O_2 \quad (10)$$

Electron paramagnetic resonance (EPR) spectra were recorded using 5,5-dimethyl-1-pyrroline *N*-oxide (DMPO) as a spin-trapping agent to prove the function of co-reaction promoters. Typical EPR signals of the DMPO-$OH^{\bullet}$ adduct with standard peaks of 1:2:2:1 and the hyperfine splitting constants of $\alpha_N \approx \alpha_{\beta\text{-H}}$ = 14.9 G were clearly observed (Figure 4D, curves b−e). The signals of DMPO-$SO_4^{\bullet-}$ were inferior to those of DMPO-$OH^{\bullet}$ due to its shorter half-time, which resulted in the difficulty to identify its sextet peaks with α_N of 13.51 G, $\alpha_{\beta\text{-H}}$ of 9.93 G, $\alpha_{\gamma\text{-H1}}$ of 1.34 G, and $\alpha_{\gamma\text{-H2}}$ of 0.88 G (Figure 4E,F, the dashed black frame).[44] Compared with Tb-MOF, Cu:Tb-MOF showed stronger signals of DMPO-$SO_4^{\bullet-}$ and DMPO-$OH^{\bullet}$ (Figure 4E, curves b,c), proving that Cu:Tb-MOF was indeed the co-reaction promoter of $S_2O_8^{2-}$. The presence of appropriate H_2O_2 increased the signal of DMPO-$SO_4^{\bullet-}$, while the signal of DMPO-$OH^{\bullet}$ remained unchanged owing to the consumption of $OH^{\bullet}$ (eq 9) (Figure 4F, curve d). When excess H_2O_2 was added into the mixture of $K_2S_2O_8$ and DMPO, the DMPO-$OH^{\bullet}$ signals were obviously enhanced and the DMPO-$SO_4^{\bullet-}$ signal slightly decreased (Figure 4F, curve e), demonstrating the scavenging of $SO_4^{\bullet-}$ by $OH^{\bullet}$ (eq 10).

Optimization of Experimental Conditions. The ECL intensity of Cu:Tb-MOF/GCE depended on the access of H_2O_2 and $S_2O_8^{2-}$ and active intermediates and the reduction of Cu:Tb-IPA, which were decided by the morphology and the size of Cu:Tb-MOF. Thus, the molar ratio of Cu^{2+} and Tb^{3+} and the reaction time for its preparation were first optimized. At the molar ratio of 1.5:1 for Cu^{2+} and Tb^{3+}, the Cu:Tb-MOF showed a relatively rough surface and a uniform particle size (Figure S3), which achieved the maximum ECL intensity at the hydrothermal reaction time of 9 h (Figure 5A,B). At the same molar ratio of Cu^{2+} and Tb^{3+}, the particle size of Cu:Tb-MOF decreased to the nanoscale with increasing reaction time (Figure S4), and the hydrodynamic diameter (Figure S5),

https://doi.org/10.1021/acs.analchem.1c03988
Anal. Chem. 2021, 93, 14878−14884

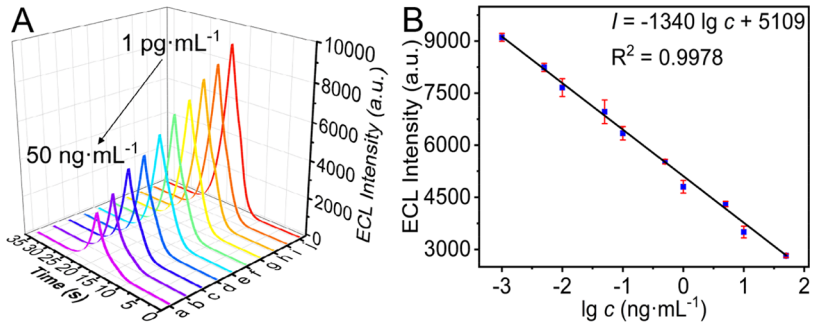

Figure 6. (A) ECL−time curves of the immunosensor at 0.001, 0.005, 0.01, 0.05, 0.1, 0.5, 1, 5, 10, and 50 ng·mL^{-1} ProGRP. (B) Calibration curve for the ECL immunoassay of ProGRP (n = 5).

nitrogen adsorption−desorption isotherm (Figure S6), and apparent area (Figure S7) of Cu:Tb-MOF also greatly depended on the reaction time (Table S1). At the reaction time of 9 h, the obtained Cu:Tb-MOF not only possessed the maximum pore diameter and volume but also exhibited relatively higher BET surface area and apparent area, which provided better access of the reactants and active intermediates to the internal ECL emitters. Therefore, Cu:Tb-MOF prepared with the molar ratio of 1.5:1 for Cu^{2+} and Tb^{3+} and the reaction time of 9 h were used to fabricate the immunosensor.

According to the ECL mechanism, the amount of Cu:Tb-MOF on the electrode surface, the pH of the detection solution, and the concentrations of both H_2O_2 and $S_2O_8^{2-}$ in the detection solution were optimized. At the Cu:Tb-MOF concentration of 2.0 mg·mL^{-1}, the obtained Cu:Tb-MOF/GCE showed the maximum ECL intensity (Figure 5C) at pH 7.4 (Figure 5D) in the presence of 100 mM $K_2S_2O_8$ (Figure 5E) and 20 mM H_2O_2 (Figure 5F). Once the concentration of H_2O_2 exceeded 20 mM, the ECL intensity decreased quickly due to the scavenging of $SO_4^{\bullet-}$ by $OH^{\bullet}$.

ECL Immunosensing Performance for ProGRP Detection. The preparation and detection processes of the ECL immunosensor were examined using electrochemical impedance spectroscopy (EIS) and the ECL intensity. Cu:Tb-MOF/GCE showed relatively low electron transfer resistance (Figure S8A, curve b). The presence of CS, antibody, BSA, and then the target protein led to a successive increase of the electron transfer resistance (Figure S8A, curves c−f), which decreased the ECL intensity of Cu:Tb-MOF (Figure S8B, curves c−f). Moreover, the ECL intensity of the immunosensor decreased obviously with the increasing concentration of ProGRP from 1.0 pg·mL^{-1} to 50 ng·mL^{-1} (Figure 6A). The plot of the ECL intensity vs the logarithm of ProGRP concentration showed good linearity (Figure 6B) with a linear equation of $I = -1340 \lg c + 5109$ (R^2 = 0.9978) and a limit of detection (LOD) of 0.68 pg·mL^{-1} at a signal-to-noise ratio of 3. Compared with other reported electrochemical immunosensors for ProGRP, the proposed immunosensor presented the widest detection range and the lowest LOD (Table S2).

The immunosensor possessed excellent operation stability. After the immunosensors were incubated with different concentrations of ProGRP, continuous cyclic scanning did not change the ECL intensity (Figure S9A). The storage stability was also acceptable. After the immunosensor was stored at 4 °C for 30 days, the ECL emission retained 92.1% of its original response (Figure S9B). Using CEA, NSE, CY211, and CA 125 as interferents, the proposed immunosensors showed good specificity toward ProGRP at even 1% concentration of interferents (Figure S9C). In addition, the relative standard deviations (RSDs) for intra- and interassay were 1.1 and 2.0%, respectively (Figure S9D), indicating favorable reproducibility. Moreover, this strategy circumvented the complicated preparation of nanomaterials and time-consuming fabrication of immunosensors, indicating its promising application in clinical diagnosis.

Real-Sample Analysis. Three serum samples of lung cancer patients were provided by a local tumor hospital with the ProGRP content of 29.1, 82.7, and 141 pg·mL^{-1}, respectively, which were obtained from commercial ECL testing. With the calibration curve shown in Figure 6B, the corresponding ProGRP levels in the serum samples were 28.3, 76.5, and 136 pg·mL^{-1} (n = 3), respectively. The detection results were comparable with the reference values (Figure S10), showing excellent detection precision.

CONCLUSIONS

This work designs an effective ECL signal amplification strategy using Cu:Tb-MOF as both the emitter and a co-reaction promoter for construction of a label-free ECL immunosensor. The morphology and size of Cu:Tb-MOF can be efficiently tuned via changing the molar ratio of Cu^{2+} and Tb^{3+} and the reaction time to achieve the maximum ECL intensity. The large pore diameter and volume, high BET surface area and apparent area, and low electron transfer resistance of the optimized Cu:Tb-MOF provide easy access of the reactants and active intermediates to the internal ECL emitters for improving the ECL emission. By introducing H_2O_2 in the ECL system, an ECL mechanism involving dual co-reaction promoters, which enhances the generation of $SO_4^{\bullet-}$ radicals for oxidizing Cu:Tb-IPA$^{\bullet-}$ formed in the cathodic process to produce more excited emitters, has been proposed to amplify the ECL emission. The excellent electrochemical and ECL behaviors of Cu:Tb-MOF lead to convenient preparation and outstanding performance of the proposed label-free ECL immunosensor. The high sensitivity, wide detection range, and stable response demonstrate the promising application prospect of lanthanide MOFs and the proposed strategy in bioassay.

ASSOCIATED CONTENT

Supporting Information

The Supporting Information is available free of charge at https://pubs.acs.org/doi/10.1021/acs.analchem.1c03988.

Materials, reagents, and apparatus; schematic diagram of the energy transfer process; energy-dispersive X-ray spectroscopy (EDS), X-ray photoelectron spectroscopy,

https://doi.org/10.1021/acs.analchem.1c03988
Anal. Chem. 2021, 93, 14878−14884

FT-IR spectroscopy, thermogravimetric analysis (TGA), XRD, SEM, dynamic light scattering (DLS), BET, CV, and EIS characterization of Cu:Tb-MOF; feasibility and performance of the ECL immunosensor; comparison among detection methods; and real-sample analysis (PDF)

AUTHOR INFORMATION

Corresponding Author

Huangxian Ju − *State Key Laboratory of Analytical Chemistry for Life Science, School of Chemistry and Chemical Engineering, Nanjing University, Nanjing 210023, P. R. China;* orcid.org/0000-0002-6741-5302; Phone: +86-25-89683593; Email: hxju@nju.edu.cn

Authors

Chao Wang − *State Key Laboratory of Analytical Chemistry for Life Science, School of Chemistry and Chemical Engineering, Nanjing University, Nanjing 210023, P. R. China*

Zhaohui Li − *College of Chemistry, Green Catalysis Center, Henan Joint International Research Laboratory of Green Construction of Functional Molecules and Their Bioanalytical Applications, Zhengzhou University, Zhengzhou 450001, P. R. China;* orcid.org/0000-0003-3946-0656

Complete contact information is available at: https://pubs.acs.org/10.1021/acs.analchem.1c03988

Notes

The authors declare no competing financial interest.

ACKNOWLEDGMENTS

The authors acknowledge the financial support of the National Natural Science Foundation of China (21890741, 21827812, and 21635005).

REFERENCES

(1) Liu, Z. Y.; Qi, W. J.; Xu, G. B. *Chem. Soc. Rev.* **2015**, *44*, 3117−3142.
(2) Chen, A. Y.; Liang, W. B.; Wang, H. J.; Zhuo, Y.; Chai, Y. Q.; Yuan, R. *Anal. Chem.* **2020**, *92*, 1379−1385.
(3) Wang, N. N.; Chen, L. Z.; Chen, W. W.; Ju, H. X. *Anal. Chem.* **2021**, *93*, 5327−5333.
(4) Yu, L.; Zhang, Q.; Kang, Q.; Zhang, B.; Shen, D. Z.; Zou, G. Z. *Anal. Chem.* **2020**, *92*, 7581−7587.
(5) Ke, H.; Zhang, X.; Guo, W. W.; Zhang, A. M.; Wang, Z. M.; Huang, C. S.; Jia, N. Q. *Talanta* **2017**, *171*, 1−7.
(6) Wu, B. N.; Miao, C. C.; Yu, L. L.; Wang, Z. Y.; Huang, C. S.; Jia, N. Q. *Sens. Actuators, B* **2014**, *195*, 22−27.
(7) Afsharan, H.; Navaeipour, F.; Khalilzadeh, B.; Tajalli, H.; Mollabashi, M.; Ahar, M. J.; Rashidi, M. R. *Biosens. Bioelectron.* **2016**, *80*, 146−153.
(8) Yang, X.; Yuan, R.; Chai, Y. Q.; Zhuo, Y.; Mao, L.; Yuan, S. R. *Biosens. Bioelectron* **2010**, *25*, 1851−1855.
(9) Feng, Y. Q.; Sun, F.; Wang, N. N.; Lei, J. P.; Ju, H. X. *Anal. Chem.* **2017**, *89*, 7659−7666.
(10) Qin, X. L.; Zhang, X. H.; Wang, M. H.; Dong, Y. F.; Liu, J. J.; Zhu, Z. W.; Li, M. X.; Yang, D.; Shao, Y. H. *Anal. Chem.* **2018**, *90*, 11622−11628.
(11) Jiang, X. Y.; Wang, Z. L.; Wang, H. J.; Zhuo, Y.; Yuan, R.; Chai, Y. Q. *Chem. Commun.* **2017**, *53*, 9705−9708.
(12) Wang, Y. F.; Li, Y. X.; Zhuang, X. M.; Tian, C. Y.; Fu, X. L.; Luan, F. *Biosens. Bioelectron.* **2021**, *190*, No. 113371.
(13) Wang, N. N.; Gao, H.; Li, Y. Z.; Li, G. M.; Chen, W. W.; Jin, Z. C.; Lei, J. P.; Wei, Q.; Ju, H. X. *Angew. Chem., Int. Ed.* **2021**, *60*, 197−201.
(14) Jin, Z. C.; Zhu, X. R.; Wang, N. N.; Li, Y. F.; Ju, H. X.; Lei, J. P. *Angew. Chem., Int. Ed.* **2020**, *59*, 10446−10450.
(15) Zhu, D.; Zhang, Y.; Bao, S. S.; Wang, N. N.; Yu, S.; Luo, R. G.; Ma, J.; Ju, H. X.; Lei, J. P. *J. Am. Chem. Soc.* **2021**, *143*, 3049−3053.
(16) Zhao, L.; Song, X. Z.; Ren, X.; Fan, D. W.; Wei, Q.; Wu, D. *Anal. Chem.* **2021**, *93*, 8613−8621.
(17) Zhao, L.; Song, X. Z.; Ren, X.; Wang, H.; Fan, D. W.; Wu, D.; Wei, Q. *Biosens. Bioelectron.* **2021**, *191*, No. 113409.
(18) Wang, Y. G.; Zhao, G. H.; Chi, H.; Yang, S. H.; Niu, Q. F.; Wu, D.; Cao, W.; Li, T. D.; Ma, H. M.; Wei, Q. *J. Am. Chem. Soc.* **2021**, *143*, 504−512.
(19) Richter, M. M.; Bard, A. J. *Anal. Chem.* **1996**, *68*, 2641−2650.
(20) Hu, L. Y.; Wu, Y.; Xu, M.; Gu, W. L.; Zhu, C. Z. *Chem. Commun.* **2020**, *56*, 10989−10999.
(21) Jiang, X. Y.; Wang, H. J.; Chai, Y. Q.; Shi, W. B.; Yuan, R. *Anal. Chem.* **2020**, *92*, 8992−9000.
(22) Lei, Y. M.; Xiao, B. Q.; Liang, W. B.; Chai, Y. Q.; Yuan, R.; Zhuo, Y. *Biosens. Bioelectron.* **2018**, *109*, 109−115.
(23) Zhou, Y.; Chen, M. X.; Zhuo, Y.; Chai, Y. Q.; Xu, W. J.; Yuan, R. *Anal. Chem.* **2017**, *89*, 6787−6793.
(24) Lei, Y. M.; Zhou, J.; Chai, Y. Q.; Zhuo, Y.; Yuan, R. *Anal. Chem.* **2018**, *90*, 12270−12277.
(25) Zeng, W. J.; Liao, N.; Lei, Y. M.; Zhao, J.; Chai, Y. Q.; Yuan, R.; Zhuo, Y. *Biosens. Bioelectron.* **2018**, *100*, 490−496.
(26) Zhang, J. L.; Yang, Y.; Liang, W. B.; Yao, L. Y.; Yuan, R.; Xiao, D. R. *Anal. Chem.* **2021**, *93*, 3258−3265.
(27) Yang, X.; Yu, Y. Q.; Peng, L. Z.; Lei, Y. M.; Chai, Y. Q.; Yuan, R.; Zhuo, Y. *Anal. Chem.* **2018**, *90*, 3995−4002.
(28) Xue, J. W.; Yang, L.; Jia, Y.; Wang, H.; Zhang, N.; Ren, X.; Ma, H. M.; Wei, Q.; Ju, H. X. *ACS Sens.* **2019**, *4*, 2825−2831.
(29) Dai, P. P.; Yu, T.; Shi, H. W.; Xu, J. J.; Chen, H. Y. *Anal. Chem.* **2015**, *87*, 12372−12379.
(30) Molina, R.; Filella, X.; Auge, J. M. *Clin. Biochem.* **2004**, *37*, 505−511.
(31) Miyake, Y.; Kodama, T.; Yamaguchi, K. *Cancer Res.* **1994**, *54*, 2136−2140.
(32) Qi, Z. W.; Wang, L.; You, Q.; Chen, Y. *Biosens. Bioelectron.* **2017**, *96*, 227−232.
(33) Wei, W. T.; Lu, Y.; Chen, W.; Chen, S. W. *J. Am. Chem. Soc.* **2011**, *133*, 2060−2063.
(34) Liu, Y. S.; Zhou, S. Y.; Tu, D. T.; Chen, Z.; Huang, M. D.; Zhu, H. M.; Ma, E.; Chen, X. Y. *J. Am. Chem. Soc.* **2012**, *134*, 15083−15090.
(35) Mi, X. N.; Sheng, D. F.; Yu, Y. E.; Wang, Y. H.; Zhao, L. M.; Lu, J.; Li, Y. W.; Li, D. C.; Dou, J. M.; Duan, J. G.; Wang, S. N. *ACS Appl. Mater. Interfaces* **2019**, *11*, 7914−7926.
(36) Li, Y.; Jiang, Z. W.; Xiao, S. Y.; Huang, C. Z.; Li, Y. F. *Anal. Chem.* **2018**, *90*, 12191−12197.
(37) Lei, Y. M.; Huang, W. X.; Zhao, M.; Chai, Y. Q.; Yuan, R.; Zhuo, Y. *Anal. Chem.* **2015**, *87*, 7787−7794.
(38) Yin, H. Q.; Yin, X. B. *Acc. Chem. Res.* **2020**, *53*, 485−495.
(39) Einkauf, J. D.; Clark, J. M.; Paulive, A.; Tanner, G. P.; de Lill, D. T. *Inorg. Chem.* **2017**, *56*, 5544−5552.
(40) Song, X. Z.; Li, X. J.; Wei, D.; Feng, R.; Yan, T.; Wang, Y. G.; Ren, X.; Du, B.; Ma, H. M.; Wei, Q. *Biosens. Bioelectron.* **2019**, *126*, 222−229.
(41) Jia, Y.; Yang, L.; Xue, J. W.; Ren, X.; Zhang, N.; Fan, D. W.; Wei, Q.; Ma, H. M. *Biosens. Bioelectron.* **2019**, *144*, No. 111676.
(42) Wang, J.; Wang, H. X.; Cao, W. N.; Zhang, Q. Q.; Zhong, W. Y. *Talanta* **2020**, *212*, 120798−120806.
(43) Yao, W.; Wang, L.; Wang, H. Y.; Zhang, X. L. *Electrochim. Acta* **2008**, *54*, 733−737.
(44) Wang, L. L.; Lan, X.; Peng, W. Y.; Wang, Z. H. *J. Hazard Mater.* **2021**, *408*, No. 124436.